Article

Highly Efficient Ag_3PO_4/g-C_3N_4 Z-Scheme Photocatalyst for Its Enhanced Photocatalytic Performance in Degradation of Rhodamine B and Phenol

Mingxi Zhang [1,2]**, Hanxiao Du** [2]**, Juan Ji** [2]**, Fengfeng Li** [2,*]**, Y. C. Lin** [1,3,*] **, Chenwei Qin** [2]**, Ze Zhang** [2] **and Yi Shen** [2]

[1]   Light Alloy Research Institute, Central South University, Changsha 410083, China; zhangmingxi@csu.edu.cn
[2]   Key Laboratory of Inorganic Nonmetallic Materials Hebei Province,
     College of Materials Science and Engineering, North China University of Science and Technology,
     Tangshan 063210, China; 13731002744@163.com (H.D.); j17732534673@163.com (J.J.);
     qincw64@hotmail.com (C.Q.); z17331243479@163.com (Z.Z.); shenyi@ncst.edu.cn (Y.S.)
[3]   School of Mechanical and Electrical Engineering, Central South University, Changsha 410083, China
*   Correspondence: lifengfeng@heuu.edu.cn (F.L.); yclin@csu.edu.cn (Y.C.L.)

Abstract: Ag_3PO_4/g-C_3N_4 heterojunctions, with different g-C_3N_4 dosages, were synthesized using an in situ deposition method, and the photocatalytic performance of g-C_3N_4/Ag_3PO_4 heterojunctions was studied under simulated sunlight conditions. The results revealed that Ag_3PO_4/g-C_3N_4 exhibited excellent photocatalytic degradation activity for rhodamine B (Rh B) and phenol under the same light conditions. When the dosage of g-C_3N_4 was 30%, the degradation rate of Rh B at 9 min and phenol at 30 min was found to be 99.4% and 97.3%, respectively. After five cycles of the degradation experiment for Rh B, g-C_3N_4/Ag_3PO_4 still demonstrated stable photodegradation characteristics. The significant improvement in the photocatalytic activity and stability of g-C_3N_4/Ag_3PO_4 was attributed to the rapid charge separation between g-C_3N_4 and Ag_3PO_4 during the Z-scheme charge transfer and recombination process.

Keywords: Ag_3PO_4; g-C_3N_4; semiconductor photocatalyst; Z-scheme mechanism

1. Introduction

With the rapid development of industry, environmental pollution caused by industrial wastewater is becoming increasingly serious. Photocatalysis is an effective technology to degrade pollutants in water, which has been widely researched [1,2]. However, one-component semiconductor photocatalysts always face various defects, such as low visible-light availability and easy recombination of photogenerated charges. It has been proven that the construction of semiconductor heterostructures is an effective route to improve photocatalytic efficiency [3,4]. In recent years, an all-solid Z-scheme semiconductor composite photocatalyst has been applied in photocatalysis [5–9]. When Z-scheme photocatalysts are excited, h^+ from the valence band (VB) at a higher energy level can combine with e^- from the conduction band (CB) at a lower energy level, while e^- with a stronger reducing ability in CB at a higher energy level and h^+ with a stronger oxidation ability in lower VB at a lower energy level can participate in the reduction and oxidation processes during photocatalytic degradation, respectively. This method is conducive to obtain high charge separation efficiency and strong redox ability simultaneously, thus improving the photocatalytic efficiency [8,9].

In recent years, Z-scheme Ag_3PO_4-based photocatalysts with a high photocatalytic activity have been designed and applied in wastewater treatment and environmental control [10–13], including Ag_3PO_4/MoS_2 [14], Bi_2MoO_6/Ag_3PO_4 [15], Ag_3PO_4/Bi_2WO_6 [16], Ag_3PO_4RGO/$BiMoO_4$ [17], $AgPO_4$/Ag/WO_{3-x} [18], and Ag_3PO_4/Pd/$LaPO_4$ [19]. Lamellar g-C_3N_4 nanosheets possess high surface area, suitable band gap (2.7 eV), low cost, and good

thermal and chemical stability, which has attracted extensive attention in the field of photocatalysis [20–23]. When g-C_3N_4 is combined with Ag_3PO_4, the resultant g-C_3N_4/Ag_3PO_4 photocatalyst is expected to show significantly enhanced photocatalytic activity.

Among the many types of pollutants, dyes and dangerous compounds are two main pollutants in industrial wastewater. Rh B and phenol are the typical substances of the two pollutants, respectively. Rh B is very harmful to human health. It can cause redness of skin and viscera, mild congestion of cerebral vascular, rupture of myocardial fiber, and other symptoms. Phenol has a strong corrosive effect on skin and mucous membrane, inhibiting the central nervous system and damaging the function of liver and kidney, etc. In addition, phenol is more difficult to degrade than other pollutants in water. Thus, they were chosen as the degradation object in photocatalytic experiments.

In this paper, we synthesized the Ag_3PO_4/g-C_3N_4 Z-scheme heterojunction photocatalyst using the in situ deposition method and evaluated the photocatalytic activity by the degradation experiment for Rh B and phenol. The influence of g-C_3N_4 and Ag_3PO_4 on photocatalytic activity was studied in detail and the probable photocatalytic mechanism of Ag_3PO_4/g-C_3N_4 was proposed.

2. Experimental Section

2.1. Sample Preparation

Preparation of g-C_3N_4: A typical calcination method was used to prepare g-C_3N_4. Briefly, 10 g urea powder was placed in an alumina crucible with a lid. The crucible was heated in air at a heating rate of 2 °C·min^{-1} to 550 °C and, then held at this temperature for 2 h to obtain g-C_3N_4. Subsequently, the bulk g-C_3N_4 was thermally exfoliated into g-C_3N_4 nanosheets by calcination at 600 °C for 2 h in air. The light yellow product was collected and ground using an agate mortar for subsequent use.

Synthesis of Ag_3PO_4/g-C_3N_4: Fifty milligrams of g-C_3N_4 nanosheets were dispersed in 80 mL of deionized water by ultrasonication. Silver ammonia solution (0.1 g·L^{-1}) was dropped into the aqueous dispersion of g-C_3N_4 nanosheets and, then magnetically stirred for 1 h to fully adsorb $Ag(NH_3)_2^{2+}$ ions on the surface of g-C_3N_4 nanosheets. Then, the KH_2PO_4 solution (0.1 g·L^{-1}) was dropped into the above mixture under magnetic agitation and the mixture continued to be stirred for 1 h. The final product was collected by centrifugation, washed with deionized water and ethanol thrice, and dried at 70 °C for 1 h. Finally, the product was collected and ground with an agate mortar for further use. According to the theoretical dosage of g-C_3N_4, the as-prepared samples were named Ag_3PO_4/g-C_3N_4-10 wt%, Ag_3PO_4/g-C_3N_4-20 wt%, Ag_3PO_4/g-C_3N_4-30 wt%, and Ag_3PO_4/g-C_3N_4-40 wt%. The actual dosage of g-C_3N_4 detected by EDS were 9.2 wt%, 16.3 wt%, 27.7 wt%, and 41.8 wt%, respectively. In addition, the simple physical mixture of Ag_3PO_4 and 30 wt% g-C_3N_4 was named the Ag_3PO_4/g-C_3N4-30% mixture.

2.2. Sample Characterization

The crystal structure was analyzed by a Bruker D8 X-ray diffractometer (XRD, Bruker, Germany), equipped with a Cu K$_\alpha$ irradiation light source (λ = 0.154 nm). The microstructure was observed using a Tecnai G2 F20 transmission electron microscopy (TEM, FEI, Hillsboro, OR, USA). Room-temperature transient photoluminescence (PL) spectra were recorded using an FLS1000 spectrometer (EI, UK). UV-vis diffuse reflectance spectra (UV-Vis, Hitachi, Tokyo, Japan) were measured by using a UH4150 UV-Vis near-infrared spectrophotometer. The photocurrent response was measured using a CHI 760E electrochemical workstation (Chenhua, Shanghai, China).

### 2.3. Photocatalytic Activity Test

The photocatalytic activity was evaluated by the pollutant degradation experiments at room temperature. A Polfilet xenon lamp (300 W) with a 320-nm filter was used as the light source. The spectra of the xenon lamp are shown in Figure S1 and detailed experimental devices are shown in Figure S2. The reaction solution consisted of 50 mL

of rhodamine B (Rh B, 5 mg·L^{-1}) or 50 mL of phenol (10 mg·L^{-1}), and the photocatalyst was 0.03 g Ag$_3$PO$_4$, g-C$_3$N$_4$, or Ag$_3$PO$_4$/g-C$_3$N$_4$. The photocatalyst was weighed and added to the reaction solution, and the reaction solution was continuously stirred in the dark for 30 min to achieve an adsorption–desorption balance between the photocatalytic material and pollutant. Subsequently, the solution was irradiated by a full-wavelength Xenon lamp, and the absorbance of the supernatant was measured at certain intervals. In the cyclic experiments, the photocatalyst was separated from the reaction system after each degradation experiment, washed with ethanol and deionized water, and re-dispersed in the newly-prepared reaction solution to repeat the degradation experiment.

3. Results and Discussion

3.1. Structural Analysis and Microstructure

Figure 1 shows the XRD patterns of Ag$_3$PO$_4$, g-C$_3$N$_4$ and Ag$_3$PO$_4$/g-C$_3$N$_4$-30 wt%. As shown in Figure 1, a strong peak appeared in the diffraction pattern of g-C$_3$N$_4$ at $2\theta = 26.5°$, corresponding to the (002) planes of g-C$_3$N$_4$ (JCPDS card no. 87-1526), which is the characteristic interlayer stacking peak of g-C$_3$N$_4$ [24]. The Ag$_3$PO$_4$ and Ag$_3$PO$_4$/g-C$_3$N$_4$-30 wt% exhibited similar XRD patterns and all strong diffraction peaks corresponded to the cubic Ag$_3$PO$_4$ phase (JCPDS card no. 06-0505). The inset provided the refined XRD patterns of Ag$_3$PO$_4$ and Ag$_3$PO$_4$/g-C$_3$N$_4$-30 wt%. Compared with Ag$_3$PO$_4$, the XRD pattern of Ag$_3$PO$_4$/g-C$_3$N$_4$ showed the characteristic peaks of g-C$_3$N$_4$; however, the peak intensities were far weaker than that of Ag$_3$PO$_4$. This may be attributed to the inferior crystallinity and lower content of well-exfoliated g-C$_3$N$_4$.
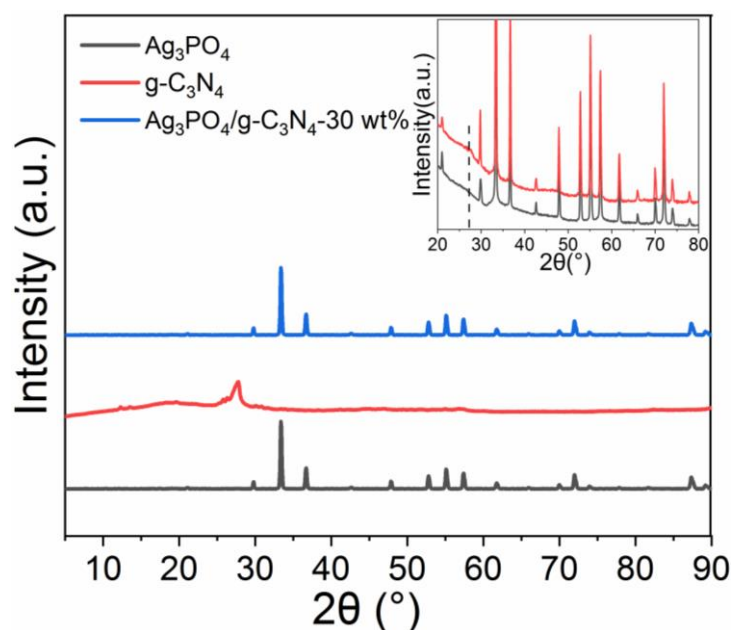
Figure 1. XRD patterns of as-prepared Ag$_3$PO$_4$, g-C$_3$N$_4$, and Ag$_3$PO$_4$/g-C$_3$N$_4$.

Figure 2 shows TEM images of Ag$_3$PO$_4$, g-C$_3$N$_4$, and Ag$_3$PO$_4$/g-C$_3$N$_4$ photocatalysts. Figure 2a illustrates that Ag$_3$PO$_4$ consisted of approximately cubic particles with a size of 200–300 nm. As shown in Figure 2b, g-C$_3$N$_4$ presented thin wrinkled nanosheets. After thermal exfoliation, the specific surface area of g-C$_3$N$_4$ increased significantly, due to morphological changes. Figure 2c shows that the small-sized Ag$_3$PO$_4$ particles were attached to the surface of g-C$_3$N$_4$, forming a stable composite.
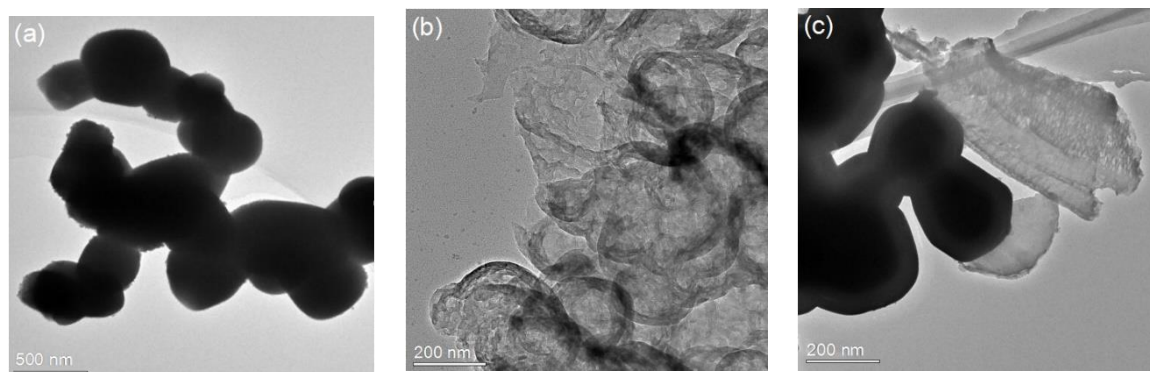
Figure 2. TEM images of (**a**) Ag_3PO_4, (**b**) g-C_3N_4, and (**c**) Ag_3PO_4/g-C_3N_4.

3.2. Optical Properties

Figure 3 shows the UV-vis diffuse reflectance spectra of Ag_3PO_4, g-C_3N_4, and Ag_3PO_4/g-C_3N_4-30 wt% photocatalysts. As shown in Figure 3a, the absorption cutoff edges of Ag_3PO_4 and g-C_3N_4 were located at about 460 and 530 nm, respectively. Compared with Ag_3PO_4, the absorption edge of Ag_3PO_4/g-C_3N_4-30 wt% was basically unchanged. Based on the UV-vis absorption data, the bandgap width of the photocatalysts was calculated and results are shown in Figure 3b. The calculated bandgap width of g-C_3N_4 was about 2.78 eV, whereas the bandgap of Ag_3PO_4 and Ag_3PO_4/g-C_3N_4-30wt% decreased to 2.45 eV.
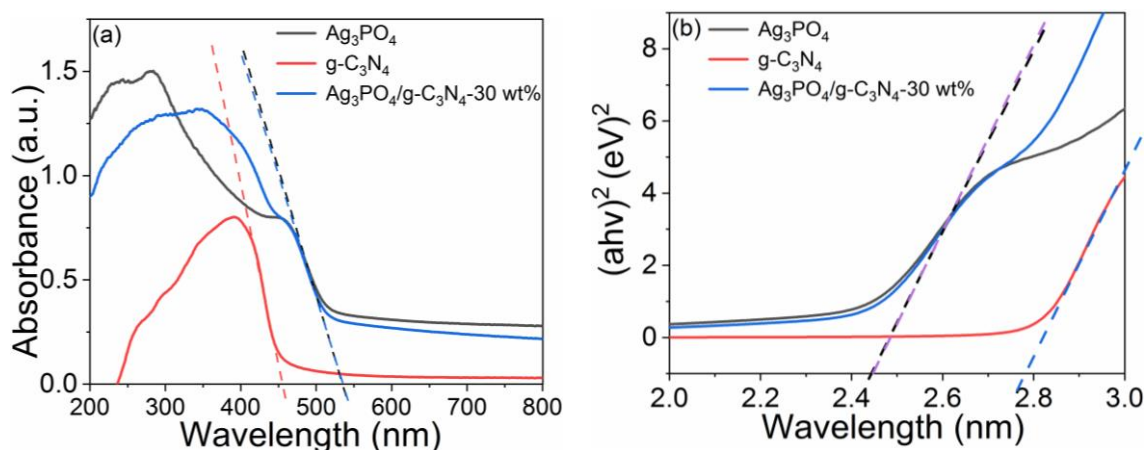
Figure 3. (**a**) UV-vis diffuse reflectance spectra, (**b**) estimated bandgap of Ag_3PO_4, g-C_3N_4, and Ag_3PO_4/g-C_3N_4-30 wt%.

By testing the photoelectrochemical properties of Ag_3PO_4, g-C_3N_4, and Ag_3PO_4/g-C_3N_4-30 wt% photocatalysts, the separation and transfer efficiency of photogenerated electron-hole pairs were studied and results are shown in Figure 4. Figure 4a presents the photoluminescence (PL) spectra of the as-synthesized photocatalysts. The PL emission peak of g-C_3N_4 was located at 460 nm, showing the highest PL intensity and indicating that the photogenerated charge of g-C_3N_4 exhibited high recombination efficiency. The PL emission peak of Ag_3PO_4 was located at 460 nm, showing a far lower PL intensity than g-C_3N_4. When Ag_3PO_4 was combined with g-C_3N_4, the location of the PL emission peak of Ag_3PO_4/g-C_3N_4-30 wt% was basically the same as Ag_3PO_4, but the PL peak intensity of Ag_3PO_4/g-C_3N_4-30 wt% was significantly lower than Ag_3PO_4. Among Ag_3PO_4, g-C_3N_4, and Ag_3PO_4/g-C_3N_4-30 wt%, Ag_3PO_4/g-C_3N_4 exhibited the lowest PL peak intensity, which corresponded to the lowest recombination efficiency for photogenerated charges. As can be observed in Figure 4b, all photocatalyst electrodes exhibited rapid response when irradiated by a Xenon lamp (full wavelength). The Ag_3PO_4/g-C_3N_4-30 wt% showed the highest photocurrent response of about 16.35 $\mu A \cdot cm^{-2}$, which was 2.79 times higher

than Ag_3PO_4 (5.87 $\mu A\cdot cm^{-2}$) and 21.8 times higher than g-C_3N_4 (0.75 $\mu A\cdot cm^{-2}$). These results indicate that the combination of Ag_3PO_4 and g-C_3N_4 reduced the recombination efficiency of photogenerated electrons and holes, and accelerated the charges transfer, which is beneficial for photocatalysis.
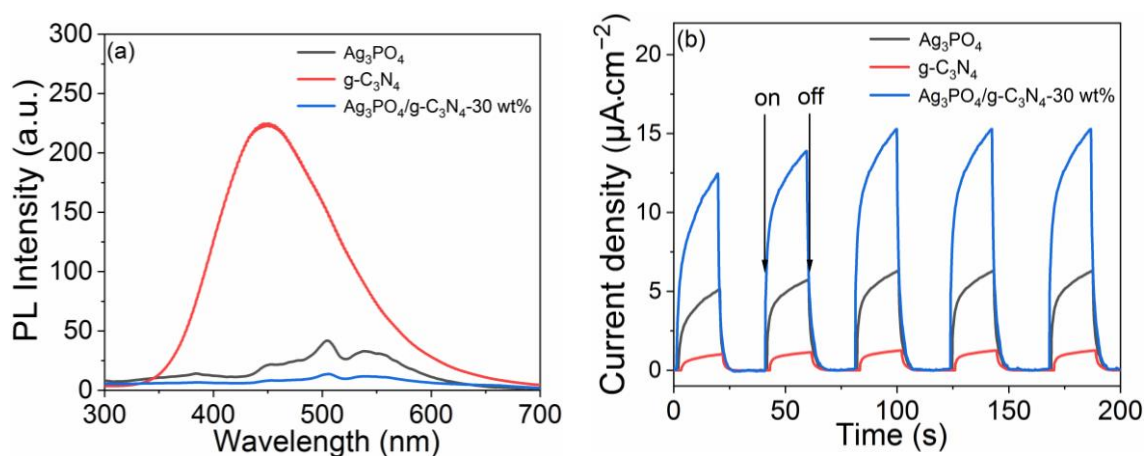
Figure 4. (**a**) Photoluminescence spectra and (**b**) transient photocurrent response curves of Ag_3PO_4, g-C_3N_4, and Ag_3PO_4/g-C_3N_4-30 wt%.

3.3. Photocatalytic Activity

Furthermore, using Rh B and phenol as target pollutants, we simulated the photocatalytic reaction under sunlight irradiation using Xenon lamp (full wavelength) irradiation, and evaluated the photocatalytic activity, as shown in Figure 5. Figure 5a shows the photocatalytic activity of Ag_3PO_4/g-C_3N_4 with different amounts of g-C_3N_4 After irradiation by the Xenon lamp for 9 min, the photocatalytic degradation rate of RhB by Ag_3PO_4, g-C_3N_4, Ag_3PO_4/g-C_3N_4-10 wt%, Ag_3PO_4/g-C_3N_4-20 wt%, Ag_3PO_4/g-C_3N_4-30 wt%, and Ag_3PO_4/g-C_3N_4-40 wt% was found to be 71.1%, 22.2%, 79.8%, 95.5%, 99.4%, and 89.9%, respectively. With the increase of g-C_3N_4 content, the photocatalytic activity of Ag_3PO_4/g-C_3N_4 initially increased, followed by a decrease. The optimal photocatalytic activity was achieved for Ag_3PO_4/g-C_3N_4-30 wt%. The first-order kinetic model [25,26] was used to calculate the corresponding reaction rate constants (k), and the results are shown in Figure 5c. The observed reaction rate constant of Ag_3PO_4, g-C_3N_4, Ag_3PO_4/g-C_3N_4-10 wt%, Ag_3PO_4/g-C_3N_4-20 wt%, Ag_3PO_4/g-C_3N_4-30 wt%, and Ag_3PO_4/g-C_3N_4-40 wt% was found to be 0.1033, 0.0209, 0.1333, 0.2591, 0.4227, and 0.1911 min^{-1}, respectively. The k value of Ag_3PO_4/g-C_3N_4-30 wt% (0.4227 min^{-1}) was the highest, which was $\approx$4.09 and 20.24 times higher than Ag_3PO_4 and g-C_3N_4, respectively.

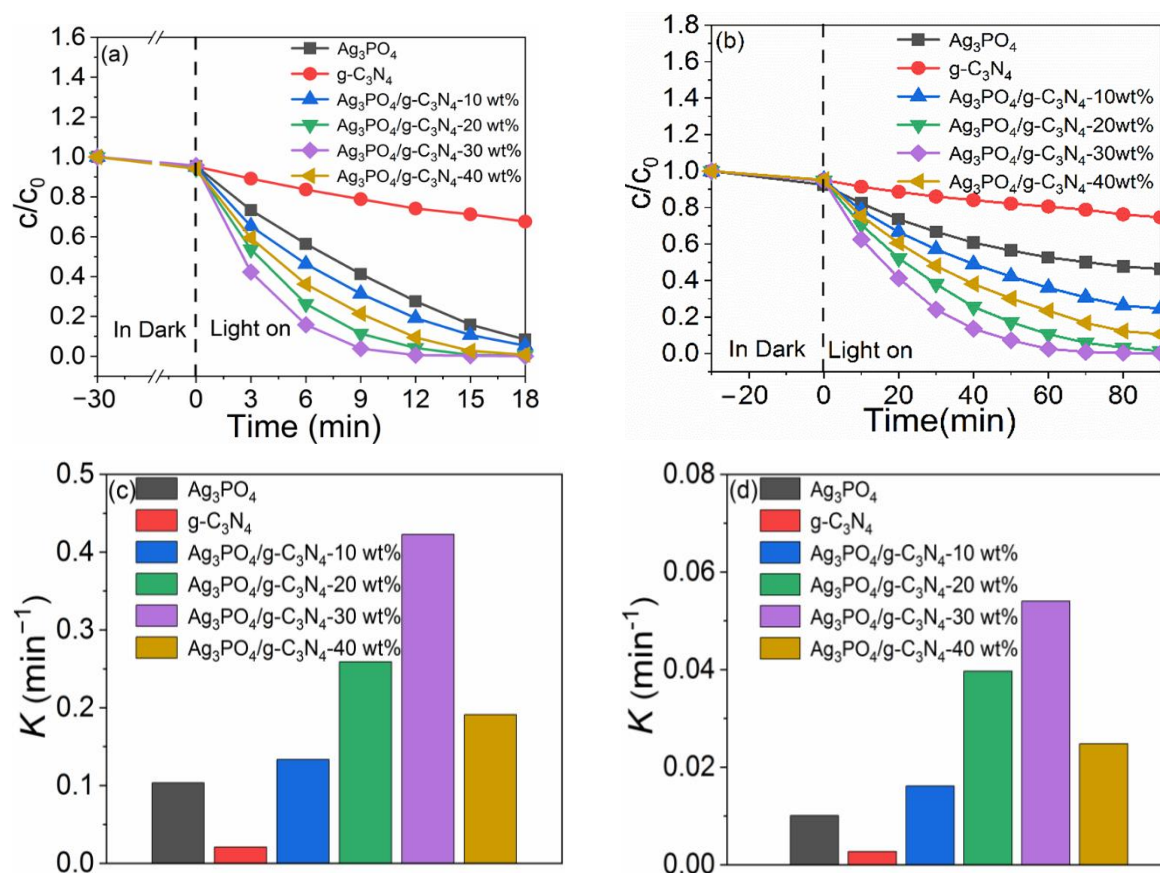**Figure 5.** (**a**,**b**) Photocatalytic curves, (**c**,**d**) rate constants in the degradation of Rh B and phenol, with different g-C$_3$N$_4$ content.

In order to further verify the superior photocatalytic activity of Ag$_3$PO$_4$/g-C$_3$N$_4$, the photocatalytic degradation experiment for phenol was also carried out and the results are shown in Figure 5b. Under Xenon lamp irradiation for 30 min, the degradation rate of phenol by Ag$_3$PO$_4$, g-C$_3$N$_4$, Ag$_3$PO$_4$/g-C$_3$N$_4$-10 wt%, Ag$_3$PO$_4$/g-C$_3$N$_4$-20 wt%, Ag$_3$PO$_4$/g-C$_3$N$_4$-30 wt%, and Ag$_3$PO$_4$/g-C$_3$N$_4$-40 wt% was found to be 43.0%, 15.8%, 63.9%, 90.9%, 99.6%, and 77.5%, respectively. Figure 5d shows that the Ag$_3$PO$_4$/g-C$_3$N$_4$-30 wt% exhibits the highest rate constant k (0.0540 min^{-1}), which was ≈5.35 and 20.00 times higher than Ag$_3$PO$_4$ (0.01009 min^{-1}) and g-C$_3$N$_4$ (0.0027 min^{-1}), respectively. Hence, Ag$_3$PO$_4$/g-C$_3$N$_4$ showed obvious advantages for the degradation of pollutants.

Figure 6 presents the cyclic stability of Rh B degradation by Ag$_3$PO$_4$, g-C$_3$N$_4$, and Ag$_3$PO$_4$/g-C$_3$N$_4$-30 wt% photocatalysts. Under Xenon lamp irradiation, the loss rate of Rh B degradation by Ag$_3$PO$_4$, g-C$_3$N$_4$, and Ag$_3$PO$_4$/g-C$_3$N$_4$-30 wt% during the fifth cycle, compared with the initial degradation, was 32.5%, 11.5%, and 7.3%, respectively. The presence of g-C$_3$N$_4$ significantly reduced the loss rate for Rh B and phenol degradation. Hence, Ag$_3$PO$_4$/g-C$_3$N$_4$ showed excellent photocatalytic stability.
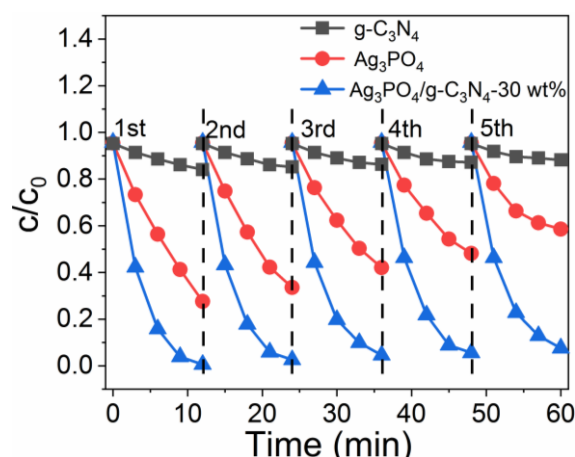
Figure 6. Recycling runs results of Ag_3PO_4, g-C_3N_4, and Ag_3PO_4/g-C_3N_4-30 wt% in degradation of Rh B.

3.4. Photocatalysis Species

In order to identify the active species during the photocatalytic process, free radical capture experiments were carried out using Rh B as a target pollutant. EDTA-2Na, p-benzoquinone (BZQ), and tert-butanol were introduced during the photocatalytic process as h^+, $\cdot O_2^-$, and OH^- inhibitors, respectively, and the results are shown in Figure 7. The introduction of tert-butanol during the photocatalytic process of Ag_3PO_4/g-C_3N_4-30 wt% rendered no influence on the photodegradation efficiency of Rh B, whereas EDTA-2Na and BZQ both significantly reduced the degradation efficiency of Rh B with a degradation rate of 4.4% and 12.4%, respectively. These results indicate that h^+ and O^{2-} are the main active species in Ag_3PO_4/g-C_3N_{4-}30 wt%.
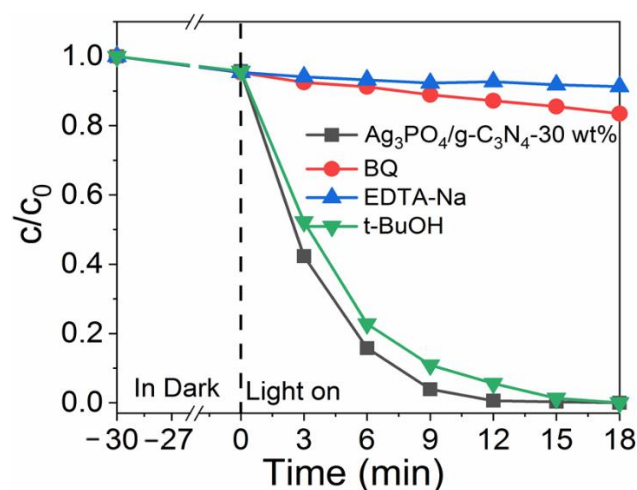
Figure 7. Photocatalytic activities of Ag_3PO_4/g-C_3N_4-30wt% for the degradation of Rh B in the presence of different scavengers.

3.5. Energy Band Structure and Photocatalytic Mechanism

Figure 8 presents the Z-scheme charge transfer pathway of the Ag_3PO_4/g-C_3N_4 composite photocatalyst for the degradation of organic pollutants. The bandgap of g-C_3N_4 was 2.7 eV with the VB potential of ~−1.4 eV and CB potential of ~−1.3 eV [27,28]. The potential of e^- on the CB of g-C_3N_4 was −1.3 eV, which can reduce the molecular oxygen O_2 to $\cdot O^2$ because the potential of O_2/$\cdot O_2^-$ was −0.44 eV vs. NHE. Therefore, O^{2-} was the main active substance during the photocatalytic process by g-C_3N_4. The bandgap of Ag_3PO_4 was 2.45 eV with a VB potential of ~2.9 eV and CB potential of ~0.45 eV [29].

The generated electrons (e^-) in the CB of Ag_3PO_4 are insufficient to reduce O_2 into O^{2-}. Therefore, holes (h^+) play a major role during the photocatalytic degradation of organic matter by Ag_3PO_4.
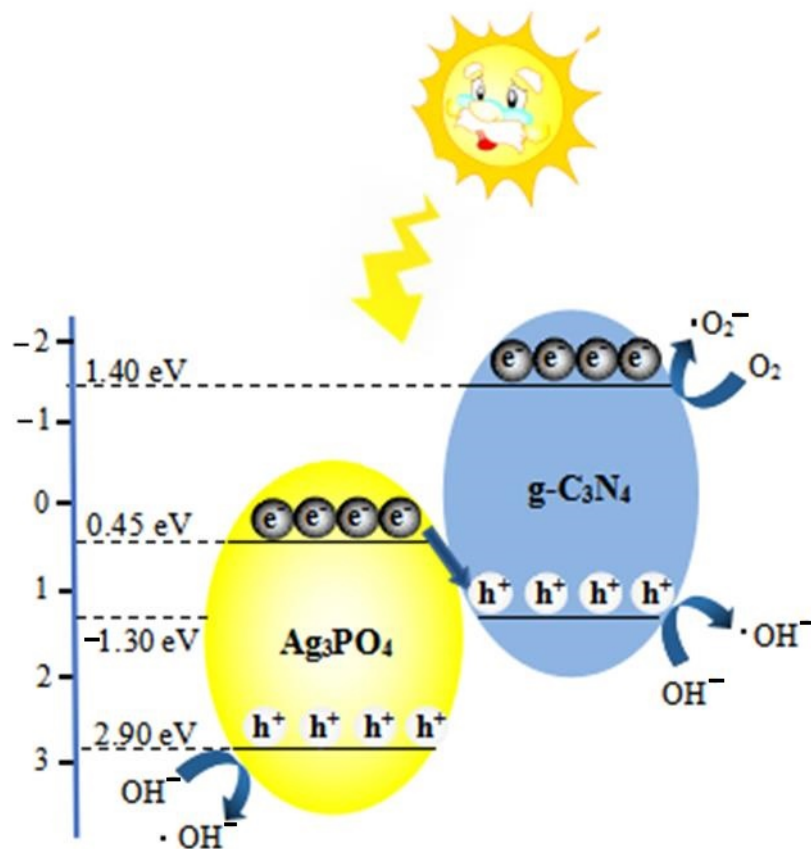

Figure 8. Energy band structure and Z-scheme photocatalytic mechanism of Ag_3PO_4/g-C_3N_4.

Based on the energy band analysis, it can be inferred that the photogenerated e^- in the CB of Ag_3PO_4 can combine with h^+ in the VB of g-C_3N_4 due to the formation of a heterojunction interface between Ag_3PO_4 particles and g-C_3N_4 nanosheets, resulting in the accumulation of e^- in the CB of g-C_3N_4 and h^+ in VB of Ag_3PO_4. The h^+ in the VB of Ag_3PO_4 can directly react with pollutants, whereas the electrons in CB of g-C_3N_4 can reduce O_2 into O^{2-}, which reacts with pollutants. The Z-scheme charge transfer mechanism promotes the separation of electron-hole pairs, slows down the photocorrosion of Ag^+, and improves photocatalyst activity and stability.

4. Conclusions

In summary, the Z-scheme heterojunction Ag_3PO_4/g-C_3N_4 photocatalyst was synthesized using an in situ deposition method and exhibited excellent photocatalytic degradation activity for Rh B and phenol under Xenon lamp irradiation. The observed rate constant (k) for the degradation of Rh B by Ag_3PO_4/g-C_3N_4 was found to be 0.4227 min^{-1}, which was 4.09 and 20.24 times higher than pure Ag_3PO_4 and g-C_3N_4, respectively. Moreover, the k value for the degradation of phenol by Ag_3PO_4/g-C_3N_4 was 0.0540 min^{-1}, which was 5.35 and 20.00 times higher than pure Ag_3PO_4 and g-C_3N_4, respectively. Overall, the formation of the Z-scheme heterojunction hindered the recombination of photogenerated electrons and holes, and accelerated the electron transfer, thus improving the activity and stability of photocatalysts.

Supplementary Materials: Figure S1: The spectra of xenon lamp, Figure S2: The picture of experimental setup.

Conflicts of Interest: The authors declare no conflict of interest. The authors had no any personal circumstances or interest that may be perceived as inappropriately influencing the representation or interpretation of reported research results. The funders had no role in the design of the study; in the collection, analyses, or interpretation of data; in the writing of the manuscript, or in the decision to publish the results.

Sample Availability: Samples of the $Ag_3PO_4/g\text{-}C_3N_4$. photocatalyst are available from the authors. However, it may be necessary to pay properly for the synthesis and mailing of samples.

References

1. Choi, J.H.; Hong, J.; Son, Y.R.; Wang, J.; Kim, H.S.; Lee, H.; Lee, H. Comparison of Enhanced Photocatalytic Degradation Efficiency and Toxicity Evaluations of CeO_2 Nanoparticles Synthesized Through Double- Modulation. *Nanomaterials* **2020**, *10*, 1543. [CrossRef] [PubMed]
2. Yoo, H.; Lee, M.; Lee, S.; Lee, J.; Cho, S.; Lee, H.; Cha, H.G.; Kim, H.S. Enhancing Photocatalytic β-O-4 Bond Cleavage in Lignin Model Compounds by Silver-Exchanged Cadmium Sulfide. *ACS Catal.* **2020**, *10*, 8465–8475. [CrossRef]
3. Byrne, J.A.; Dunlop, P.S.M.; Hamilton, J.W.J.; Fernandez-Ibanez, P.; Polo-Lopez, I.; Sharma, P.K.; Vennard, A.S.M. A review of heterogeneous photocatalysis for water and surface disinfection. *Molecules* **2015**, *20*, 5574–5615. [CrossRef] [PubMed]
4. Wang, H.L.; Zhang, L.S.; Chen, Z.G.; Hu, J.Q.; Li, S.J.; Wang, Z.H.; Liu, J.S.; Wang, X.C. Semiconductor heterojunction photocatalysts: Design, construction, and photocatalytic performances. *Chem. Soc. Rev.* **2014**, *43*, 5234–5244. [CrossRef] [PubMed]
5. Rong, X.; Chen, H.; Rong, J.; Zhang, X.; Wei, J.; Liu, S.; Zhou, X.; Xu, J.; Qiu, F.; Wu, Z. An all-solid-state Z-scheme $TiO_2/ZnFe_2O_4$ photocatalytic system for the N_2 photofixation enhancement. *Chem. Eng. J.* **2019**, *371*, 286–293. [CrossRef]
6. Qi, K.; Cheng, B.; Yu, J.; Ho, W. A review on TiO_2-based Z-scheme photocatalysts. *Chin. J. Catal.* **2017**, *38*, 1936–1955. [CrossRef]
7. Kumar, A.; Raizada, P.; Singh, P.; Saini, R.V.; Saini, A.K.; Hosseini-Bandegharaei, A. Perspective and status of polymeric graphitic carbon nitride based Z-scheme photocatalytic systems for sustainable photocatalytic water purification. *Chem. Eng. J.* **2020**, *391*, 123496. [CrossRef]
8. Xu, Q.; Zhang, L.; Yu, J.; Wageh, S.; Al-Ghamdi, A.A.; Jaroniec, M. Direct Z-scheme photocatalysts: Principles, synthesis, and applications. *Mater. Today* **2018**, *21*, 1042–1063. [CrossRef]
9. Shi, Y.; Chen, J.; Mao, Z.; Bradley, D.; Fahlman, C.; Wang, D. Construction of Z-scheme heterostructure with enhanced photocatalytic Hoevolution for g-C_3N_4 nanosheets via loading porous silicon. *J. Catal.* **2017**, *356*, 22–31. [CrossRef]
10. Chen, X.; Dai, Y.; Wang, X. Methods and mechanism for improvement of photocatalytic activity and stability of Ag_3PO_4: A review. *J. Alloys Compd.* **2015**, *649*, 910–932. [CrossRef]
11. Ge, M.; Li, Z. Recent progress in Ag_3PO_4-based all-solid-state Z-scheme photocatalytic systems. *Chin. J. Catal.* **2017**, *38*, 1794–1803. [CrossRef]
12. Martin, D.J.; Liu, G.; Moniz, S.J.A.; Bi, Y.; Beale, A.M.; Ye, J.; Tang, J. Efficient visible driven photocatalyst, silver phosphate: Performance, understanding and perspective. *J. Alloys Compd.* **2015**, *649*, 910–932. [CrossRef] [PubMed]
13. Lang, X.; Chen, X.; Zhao, J. Heterogeneous visible light photocatalysis for selective organic transformations. *Chem. Soc. Rev.* **2015**, *44*, 7808–7828. [CrossRef]
14. Zhu, C.; Zhang, L.; Jiang, B.; Zheng, J.; Hu, P.; Li, S.; Wu, M.; Wu, W. Fabrication of Z-scheme Ag_3PO_4/MoS_2 composites with enhanced photocatalytic activity and stability for organic pollutant degradation. *Appl. Surf. Sci.* **2016**, *377*, 99–108. [CrossRef]

15. Wang, Z.; Lv, J.; Dai, K.; Lu, L.; Liang, C.; Geng, L. Large scale and facile synthesis of novel Z-scheme Bi_2MoO_6/Ag_3PO_4 composite for enhanced visible light photocatalyst. *Mater. Lett.* **2016**, *169*, 250–253. [CrossRef]

16. Wang, Z.; Hu, T.; Dai, K.; Zhang, J.; Liang, C. Construction of Z-scheme Ag_3PO_4/Bi_2WO_6 composite with excellent visible-light photodegradation activity for removal of organic contaminants. *Chin. J. Catal.* **2017**, *38*, 2021–2029. [CrossRef]

17. Zhu, P.; Chen, Y.; Duan, M.; Ren, Z.; Hu, M. Construction and mechanism of a highly efficient and stable Z-scheme Ag_3PO_4/reduced graphene oxide/$BiMoO_4$ visible-light photocatalyst. *Catal. Sci. Technol.* **2018**, *8*, 3818–3832. [CrossRef]

18. Bu, Y.; Chen, Z.; Sun, C. Highly efficient Z-Scheme $AgPO_4/Ag/WO_{3-x}$ photocatalyst for its enhanced photocatalytic performance. *Appl. Catal. B Environ.* **2015**, *179*, 363–371. [CrossRef]

19. Chen, X.; Zhang, W.; Zhang, L.; Feng, L.; Wen, J.; Yang, J.; Zhang, C.; Jiang, J.; Wang, H. An urchin-like $Ag_3PO_4/Pd/LaPO_4$ photocatalyst with Z-scheme heterojunction for enhanced hydrogen evolution. *Appl. Surf. Sci.* **2019**, *497*, 143771. [CrossRef]

20. Ren, Y.; Zeng, D.; Ong, W. Interfacial engineering of graphitic carbon nitride g-C_3N_4-based metal sulfide heterojunction photocatalysts for energy conversion: A review. *Chin. J. Catal.* **2019**, *40*, 289–319. [CrossRef]

21. Ong, W.; Tan, L.; Ng, Y.H.; Yong, S.; Chai, S. Graphitic Carbon Nitride (g-C3N4)—Based Photocatalysts for Artificial Photosynthesis and Environmental Remediation: Are We a Step Closer To Achieving Sustainability? *Chem. Rev.* **2016**, *116*, 7159–7329. [CrossRef] [PubMed]

22. Li, Y.; Yang, L.; Don, G.; Ho, W. Mechanism of NO Photocatalytic Oxidationon g-C_3N_4 Was Changed by Pd-QDs Modification. *Molecules* **2015**, *21*, 36–45. [CrossRef] [PubMed]

23. Groenewolt, M.; Antonietti, M. Synthesis of g-C_3N_4 Nanoparticles in Mesoporous Silica Host Matrices. *Adv. Mater.* **2010**, *17*, 1789–1792. [CrossRef]

24. Xu, L.; Shen, X.; Wu, J.; Ji, Z.; Wang, J.; Kong, L.; Liu, M.; Song, C. Fabrication of an all solid Z-scheme photocatalyst g-C_3N_4/GO/AgBr with enhanced visible light photocatalytic activity. *Appl. Catal. A Gen.* **2017**, *5*, 104–113.

25. Chen, X.; Li, R.; Pan, X.; Huang, X.; Yi, Z. Fabrication of In_2O_3-Ag-Ag_3PO_4 composites with Z-scheme configuration for photocatalytic ethylene degradation under visible light irradiation. *Chem. Eng. J.* **2017**, *320*, 644–652. [CrossRef]

26. Liu, L.; Ding, L.; Liu, Y.; An, W.; Lin, S.; Liang, Y.; Cui, W. A stable Ag_3PO_4@PANI core@shell hybrid: Enrichment photocatalytic degradation with r-r conjugation. *Appl. Catal. B Environ.* **2017**, *201*, 92–104. [CrossRef]

27. Rawool, S.A.; Samanta, A.; Ajithkumar, T.G.; Kar, Y.; Polshettiwar, V. Photocatalytic Hydrogen Generation and CO_2 Conversion Using g-C_3N_4 Decorated Dendritic Fibrous Nanosilica: Role of Interfaces between Silica and g-C_3N_4. *ACS Appl. Energy Mater.* **2020**, *3*, 8150–8158. [CrossRef]

28. Wei, Z.; Liang, F.; Liu, Y.; Luo, W.; Wang, J.; Yao, W.; Zhu, Y. Photoelectrocatalytic degradation of phenol-containing wastewater by TiO2/g-C3N4 hybrid heterostructure thin film. *Appl. Catal. B Environ.* **2017**, *201*, 600–606. [CrossRef]

29. Yi, Z.; Ye, J.; Kikugawa, N.; Kako, T.; Ouyang, S.; Stuart-Williams, H.; Yang, H.; Cao, J.; Luo, W.; Li, Z.; et al. An orthophosphate semiconductor with photooxidation properties under visible-light irradiation. *Nat. Mater.* **2010**, *9*, 559–564. [CrossRef]